



**HAL**  
open science

## **Dynamical Mechanical Analysis and Micromechanics Simulations of Spin-Crossover@Polymer Particulate Composites: Toward Soft Actuator Devices**

Seyed Ehsan Alavi, Baptiste Martin, Yue Zan, Xinyu Yang, Mario Piedrahita-Bello, William Nicolazzi, J.F. Ganghoffer, Lionel Salmon, Gábor Molnár, Azzedine Bousseksou

### ► To cite this version:

Seyed Ehsan Alavi, Baptiste Martin, Yue Zan, Xinyu Yang, Mario Piedrahita-Bello, et al.. Dynamical Mechanical Analysis and Micromechanics Simulations of Spin-Crossover@Polymer Particulate Composites: Toward Soft Actuator Devices. *Chemistry of Materials*, 2023, 35 (8), pp.3276-3289. 10.1021/acs.chemmater.3c00293 . hal-04104652

**HAL Id: hal-04104652**

**<https://hal.science/hal-04104652v1>**

Submitted on 24 May 2023

**HAL** is a multi-disciplinary open access archive for the deposit and dissemination of scientific research documents, whether they are published or not. The documents may come from teaching and research institutions in France or abroad, or from public or private research centers.

L'archive ouverte pluridisciplinaire **HAL**, est destinée au dépôt et à la diffusion de documents scientifiques de niveau recherche, publiés ou non, émanant des établissements d'enseignement et de recherche français ou étrangers, des laboratoires publics ou privés.

# Dynamical Mechanical Analysis and Micromechanics Simulations of Spin-Crossover@Polymer Particulate Composites: Towards Soft Actuator Devices

Seyed Ehsan Alavi,<sup>a#</sup> Baptiste Martin,<sup>a#</sup> Yue Zan,<sup>a</sup> Xinyu Yang,<sup>a</sup> Mario Piedrahita-Bello,<sup>a</sup> William Nicolazzi,<sup>a</sup> Jean-François Ganghoffer,<sup>b</sup> Lionel Salmon<sup>a\*</sup>, Gábor Molnár<sup>a\*</sup>, Azzedine Bousseksou<sup>a\*</sup>

<sup>a</sup> LCC, CNRS & Université de Toulouse, 205 route de Narbonne 31077 Toulouse, France

<sup>b</sup> LEM3. Université de Lorraine, CNRS. 7, rue Félix Savart, 57070 Metz, France

#These authors contributed equally

\*Corresponding authors: lionel.salmon@lcc-toulouse.fr, gabor.molnar@lcc-toulouse.fr, azzedine.bousseksou@lcc-toulouse.fr

**ABSTRACT:** We investigated the interplay between the thermomechanical and spin crossover (SCO) properties of a series of stimuli-responsive polymer composites consisting of  $[\text{Fe}(\text{NH}_2\text{trz})_3]\text{SO}_4$  and  $[\text{Fe}(\text{Htrz})(\text{trz})_2]\text{BF}_4$  particles (trz = 1,2,4-triazolato) embedded in thermoplastic polyurethane, TPU, and poly(vinylidene fluoride - trifluoroethylene), P(VDF-TrFE) matrices. The effective thermoelastic coefficients, transformation stress and strain in the composites were assessed utilizing dynamical mechanical analysis (DMA), differential scanning calorimetry (DSC), thermal expansion and thermal stress measurements. Remarkably, the composites display a characteristic elastic softening and increased mechanical damping around the spin transition temperature, which arise from the significant spin state - volume strain coupling in the particles and scale semi-quantitatively with the pressure derivative of the low spin fraction  $\left(\frac{\partial n}{\partial P}\right)_T$ . Crucially, for a given particle volume fraction, the transformation strain (resp. stress) substantially increases (resp. decreases) in soft matrices, which was rationalized by micromechanical simulations. The results provide a fundamental understanding and a quantitative guideline for the design of SCO@polymer composites for applications in mechanical transducers.

## 1. INTRODUCTION

Spin crossover (SCO) complexes of  $3d^4$ - $3d^7$  transition metal ions are a prominent class of switchable molecular materials capable of undergoing a reversible transformation between two spin states of the metal center via thermal, chemical, photonic and/or mechanical stimuli.<sup>1-4</sup> Specifically, at high temperature the high spin (HS) form is favored with respect to the low spin (LS) state due to its higher entropy. This change of electronic configuration is also associated with a volume change of the crystal lattice, typically of ~1-10 % (up to 22 %).<sup>5-8</sup> Because of this large transformation strain, in the past decade, SCO compounds have been increasingly considered as mechanical transducers in sensors, actuators and energy harvester devices.<sup>9-10</sup> In order to provide an engineering solution, SCO materials are usually processed either as polycrystalline coatings<sup>11-12</sup> or as particulate composites<sup>13</sup>, mostly in polymer matrices. The dispersion of SCO particles inside polymers not only increases the processability of the materials, but can also be the source of unprecedented properties thanks to the strain-driven coupling between the particles and the matrix. Hence, efforts into SCO composite mechanics have focused on utilizing the spin transition phenomenon in two ways – generating movement in actuators<sup>14-21</sup> and creating strain-coupled hybrid materials that combine the characteristics of the constituents to achieve novel functionalities,<sup>22-29</sup> notably, transduction between heat and electrical energy.<sup>30-34</sup>

SCO@polymer composite actuators were first conceived by Shepherd et al.<sup>14</sup> in the form of bilayer beams. In this initial investigation, SCO particles were embedded in a polymethylmethacrylate (PMMA) matrix, and the obtained SCO@PMMA film was then covered by an inert polyvinylpyrrolidone (PVP) layer. The resulting bimorph actuators generated significant movement upon heating, in large excess with respect to ordinary thermal expansion. In addition, the actuating properties could be tuned straightforwardly by changing the SCO-active material. Subsequent efforts focused on integrating electrothermal heating elements into the bimorph beams,<sup>15</sup> characterizing their actuation response,<sup>19-21</sup> and developing appropriate closed-loop control methods.<sup>35</sup> Beyond simple engineering configurations (e.g., rods, beams), SCO@polymer composite actuators have also been successfully shaped into more complex forms by 3D printing,<sup>16</sup> and integrated into more sophisticated structures, such as microelectromechanical systems (MEMS).<sup>17-18</sup>

Based on these studies, within the vast portfolio of emerging soft actuator materials,<sup>36-47</sup> SCO@polymer actuators appear remarkable for their vast compositional versatility, multifunctionality, ample movements, good controllability and robustness. Nevertheless, their

further development requires a deep understanding of the complex thermomechanics governing the desired function. The effect of the large strain energy density associated with the SCO in the particles (up to a few tens of  $\text{Jcm}^{-3}$ ) is of particular interest.<sup>9</sup> The resulting deformation of the composite materials, the generated stress and the variation of its thermoelastic properties must be investigated experimentally and analyzed by appropriate modeling. Initial experimental efforts towards this aim revealed sizeable changes in the elastic moduli at the spin transition (a few tens of percent), significant damping under dynamic loadings, large linear strains (up to 7 %) and relatively small thermal stresses ( $\sim\text{MPa}$  range).<sup>48-51</sup> However, the analysis and interpretation of these results has remained rather qualitative (i) for the lack of knowledge of thermoelastic properties of the SCO particles and (ii) for the lack of appropriate modeling methodology.

The primary aim of the present investigation is to provide a more comprehensive, combined experimental - modelling approach for a deeper understanding of the mechanics of SCO@polymer composites and, as a result, for an advanced design and optimization of actuator devices. An essential input for this endeavor comes from our recent investigation of thermoelastic properties of nanocrystalline powders of the technologically relevant SCO complexes  $[\text{Fe}(\text{NH}_2\text{trz})_3]\text{SO}_4$  (**1**) and  $[\text{Fe}(\text{Htrz})(\text{trz})_2]\text{BF}_4$  (**2**) (trz = triazolato), providing us the bulk transformation strain, thermal expansion coefficients, elastic moduli, and their temperature dependence.<sup>52</sup> For the present work, these powders were embedded into P(VDF<sub>80</sub>-TrFE<sub>20</sub>) and TPU matrices at different concentrations (0 - 50 wt. %). We choose these matrices for their substantially different elastic moduli ( $\sim 1$  GPa vs.  $\sim 10$  MPa), which is a crucial parameter for optimizing the actuating properties (*vide infra*). In addition, these polymers and their composites can be easily processed by blade casting, affording homogeneous particle dispersions within large sample volumes, which are required for mechanical testing.<sup>19,21</sup> It is also worth noting that the selected polymers do not exhibit any significant thermally-induced phenomena (e.g. relaxations or phase transitions) near the SCO temperatures of **1** and **2**, avoiding thus potential complications from overlapping mechanical spectroscopy signals. This issue is particularly important for the P(VDF-TrFE) matrix, which is a ferroelectric polymer exhibiting intricate electromechanical properties on its own. Indeed, one of the reasons to use the 80%-20% VDF-TrFE copolymer in this work is that it exhibits a high Curie temperature (ca. 135 °C) avoiding thus possible ‘crosstalk’ between the Curie transition and the spin transition in the composites.<sup>33-34</sup>

The manuscript is organized as follows. Section 2 provides details on sample preparation and analysis methods. Section 3 gathers the main experimental results, including sample

characterization by DSC, SEM and DMA with special focus on the temperature dependence of the elastic modulus of the composites as well as on the transformation stress and strain imparted by the SCO particles. In section 4.1 we use a thermodynamical approach of regular solutions to rationalize the pronounced elastic softening and mechanical damping observed at the spin transition. Finally, in section 4.2, we put in place a micromechanical model for the quantitative analysis of the SCO induced transformation stress and strain in the composites. The micromechanical homogenization approach we use here is based on general principles introduced by Hill<sup>53-54</sup>, which were adapted by Rosen and Hashin<sup>55</sup> for computing the effective thermal expansion coefficients of multiphase materials and by McMeeking<sup>56</sup> for phase changing particles embedded in a matrix.

## 2. METHODS

**2.1. Sample fabrication.** The synthesis and characterization of SCO particles of **1** and **2** were described in ref. 16 and 57, respectively. P(VDF-TrFE) with a VDF:TrFE molar ratio of 80:20 was provided by Piezotech, whereas TPU 85a was purchased from BASF. (See Scheme S1 in the Supporting Information, SI, for the chemical structures.) The SCO@P(VDF-TrFE) and SCO@TPU composites were blade cast with different particle concentrations (0, 15, 30 and 50 wt. %, see Table 1) using the protocols reported in ref. 19 and 21, respectively.

**Table 1.** Sample compositions.

Mass Content (wt. %)	Volume fraction in TPU	Volume fraction in P(VDF-TrFE)	Volume fraction in P(VDF-TrFE)
		[Fe(NH <sub>2</sub> trz) <sub>3</sub> ]SO <sub>4</sub>	[Fe(Htrz)(trz) <sub>2</sub> ]BF <sub>4</sub>
15	0.08	0.14	0.14
30	0.16	0.28	0.28
50	0.27	0.47	0.47

**2.2. Sample characterization.** DSC thermograms were acquired using a Netzsch DSC 3500 Sirius instrument with a heating/cooling ramp of  $\pm 10$  °C/min and a nitrogen gas purge of 20 mL/min. Temperature and enthalpy were calibrated using the melting transition of indium. Particle morphology was investigated by transmission electron microscopy (TEM) using a JEOL JEM-1011 instrument. TEM samples were prepared by placing a drop of the particles suspended in ethanol on a carbon-coated copper grid. Scanning electron microscopy (SEM)

images of the composites were obtained by means of a HITACHI S-4800 electronic microscope operated in secondary electron mode. The composite films were fractured at liquid nitrogen temperature and covered by a thin layer of Pt to study both their cross-section and surface by SEM. The film thickness was assessed using a Mitutoyo precision micrometer.

**2.3. Mechanical property analysis.** Dynamic and static uniaxial tensile measurements were carried out using a DMA850 instrument (TA Instruments), providing resolutions of force to  $10^{-5}$  N, displacement to 0.1 nm and phase lag to  $10^{-5}$  deg. Thermal expansion and thermal stress measurements were carried out in constant force and constant strain modes, respectively, between 15 - 95 °C (15 - 115 °C for composites of **2**) at a heating/cooling rate of  $\pm 1$  °C.min<sup>-1</sup>. DMA measurements were conducted between 15 and 95 °C (15 - 115 °C for composites of **2**) at a heating/cooling rate of  $\pm 3$  °C.min<sup>-1</sup> using an initial static force of 0.1 N, which was continuously adjusted, proportional to the sample stiffness variation, to ensure the dynamical force remains inferior to the static force all along the experiments. From the DMA measurements, we assessed the static elongation ( $\Delta l_s$ ) and the dynamical elongation modulus ( $E^*$ ) as a function of the temperature. The modulus was measured in displacement control mode with an imposed sinusoidal strain of 1 Hz in frequency and 0.08 % in amplitude (except otherwise stated). Before the measurements, a preliminary stress-strain measurement was carried out to ensure the oscillation amplitude remained within the linear elastic range. Each sample was measured through (at least) two thermal cycles and for two different synthesis batches to verify the reproducibility of the results. From the dynamical data, we then extracted the storage and loss moduli ( $E'$  and  $E''$ , respectively) defined by:

$$E^*(T) = E'(T) + iE''(T) = \frac{F_D}{\Delta l_D} \left( \frac{l}{wh} \right) \cos \delta + i \frac{F_D}{\Delta l_D} \left( \frac{l}{wh} \right) \sin \delta \quad (1)$$

where  $\Delta l_D$  is the amplitude of dynamic elongation of the sample,  $F_D$  is the applied dynamic force amplitude,  $\delta$  is the phase difference between the imposed strain and the resulting stress, whereas  $l$ ,  $w$ , and  $h$  are the initial length, width and thickness of the composite film, respectively. In our experiments, we used rectangular samples with typical values of  $l$ ,  $w$ , and  $h$  equal to 10, 8, and 0.05 mm, respectively. In order to inspect the possible anisotropy of the mechanical properties, several specimens were cut from each blade-cast sample with their length either parallel (//) or perpendicular ( $\perp$ ) to the direction of the blade movement (see Scheme S2).

### 3. EXPERIMENTAL RESULTS

In the following sections, we will show the results obtained with ‘parallel cut’ samples of the series **1**@P(VDF-TrFE)<sup>//</sup> and **1**@TPU<sup>//</sup>, whereas data obtained for the ‘perpendicular cut’ samples as well as for the **2**@P(VDF-TrFE) samples are provided in the SI.

**3.1. Sample characterization.** The SCO properties of the composites and neat particle powders were assessed using DSC (Fig. S1-S2 and Table S1) and variable temperature optical reflectivity measurements (Fig. S3) conducted for multiple heating-cooling cycles. Following the first heating, which is always anomalous to some extent, the SCO behavior of the samples becomes well reproducible on thermal cycling. Between the SCO behavior of the neat powders and the composites no substantial difference can be observed. As an example, Fig. 1 compares the DSC thermograms of the neat powder of **1** with that of the composites **1**@P(VDF-TrFE) and **1**@TPU for 50 wt. % particle concentration. The powder of **1** displays an endothermic (exothermic) peak around 72 °C (52 °C) on heating (cooling), denoting a ca. 20 K wide thermal hysteresis in agreement with the first-order nature of the transition. (Note that the apparent hysteresis widths are somewhat different in the DSC, thermorefectance and DMA measurements due to the different heat transfer conditions.) The excess enthalpy associated with the spin transition in **1** is  $48.2 \pm 0.2$  J/g. In the case of the composites, the DSC peaks associated with the SCO are comparable with the thermogram of the powder (Fig. 1). In particular, both the transition temperatures and enthalpies (scaled for the same particle weight) remain nearly unaffected by the presence of the polymer matrix (see also Table S1 and Fig. S1-S2). Interestingly, for the P(VDF-TrFE) (resp. TPU) composites, we observed systematically a small downshift (resp. upshift) of the transition temperature in the heating (resp. cooling) branch of the hysteresis. This slight, but significant reduction of the hysteresis width indicates possible changes of the free energy barrier to the nucleation of the HS (resp. LS) phases in the composites in comparison to the neat powder. Overall, we can say, however, that the SCO properties remain well preserved in the different investigated composites.

In agreement with our previous results,<sup>21,57</sup> TEM observations confirmed that compound **1** forms well-defined, rod-shaped particles with lengths of 1-2  $\mu\text{m}$  and an aspect ratio of ca. 10, whereas particles of **2** display irregular and polydisperse morphology with an average particle size of ca. 50 nm (see Fig. S4). The good dispersion of the particles in the polymer matrices was verified using SEM (see Fig. 2 and Fig. S5). In both matrices, the rod-shaped particles of **1** appear partially aligned along the blade-casting direction. This finding is also corroborated by the observed anisotropy of the mechanical properties of composites of **1** (*vide infra*). For the small, irregularly shaped particles of **2**, preferential orientation cannot be detected by SEM – in

agreement with the fact that the mechanical properties were found independent of the direction in which the tensile specimens were cut from the blade-cast film (*vide infra*).

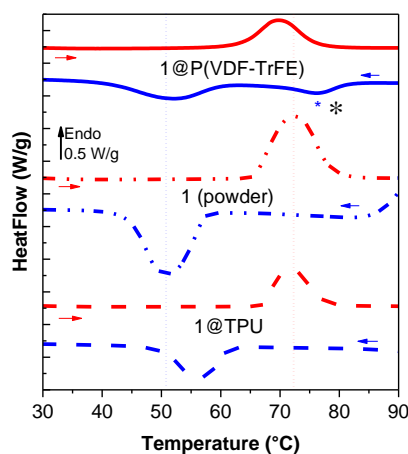


**Fig. 1.** Representative DSC thermograms (second thermal cycle) of the powder of **1** compared to **1@P(VDF-TrFE)** and **1@TPU** (50 wt.%). Arrows show heating (red) and cooling (blue). (In the P(VDF-TrFE) composites the Curie peak of the copolymer is marked by a \* symbol.)

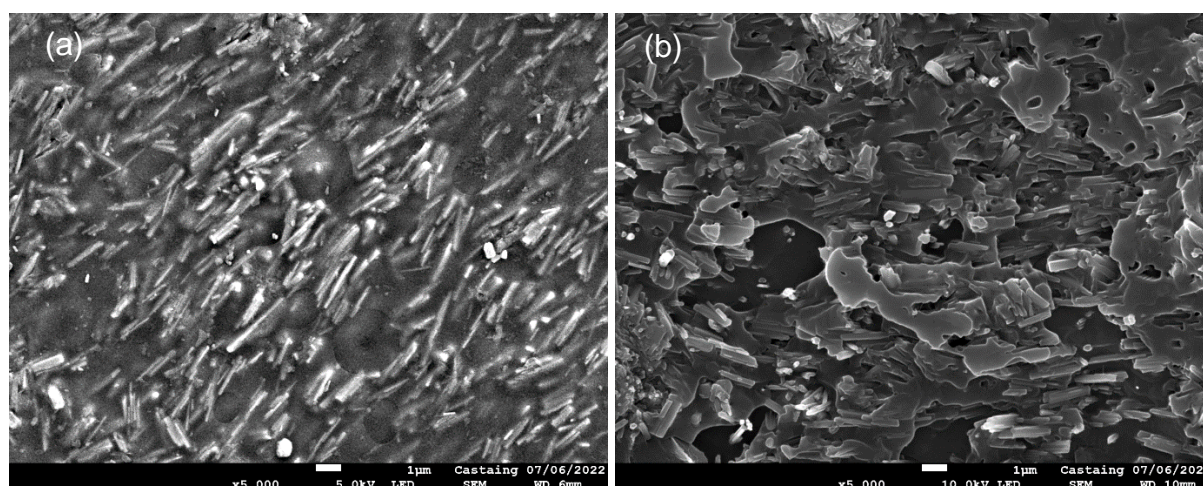


**Fig. 2.** Representative SEM images of a **1@TPU** sample (a) surface and (b) cross-section.

**3.2. Dynamic elongation modulus of the composites.** The temperature dependence of the storage and loss moduli of the **1@P(VDF-TrFE)**<sup>//</sup> and **1@TPU**<sup>//</sup> composite films is displayed in Figures 3 and 4, respectively, for different particle concentrations. For comparison, the thermomechanical behavior of the pure polymers is also shown. The storage modulus of the pure P(VDF-TrFE) films near room temperature is *ca.* 650 MPa, which decreases steadily to a value of *ca.* 80 MPa at 90 °C. The loss modulus displays a similar tendency with values between *ca.* 60 and 15 MPa in the investigated temperature range. As it can be expected, loading the polymer with stiff SCO particles increases both  $E'$  and  $E''$  (see also Table 2), except for the highest particle volume fractions (*ca.* 0.5) for which particle aggregation may prevail. (*N.B.* It may be worth to recall here that the bulk moduli of **1** and **2** are *ca.* 13 and 20 GPa,



respectively.<sup>52</sup>) The most apparent mechanical effect in the composites is a storage modulus dip, denoting elastic softening, and a concomitant loss modulus peak, denoting enhanced mechanical damping. One can also note a more or less pronounced asymmetry of both phenomena. These elastic anomalies appear close to the SCO temperatures, seen in DSC, and their amplitude clearly correlates with the particle concentration – confirming unambiguously that they arise due to the SCO phenomenon. These patterns of storage and loss moduli are very similar in all investigated samples, including the TPU composites (Fig. 4), composites of compound **2** (Fig. S6) as well as the ‘perpendicular cut’ samples (Figs. S7-S9). Nevertheless, it is interesting to notice that the elastic anomalies are systematically smaller in the ‘perpendicular cut’ samples of composites of **1**, reflecting the preferential particle orientation.

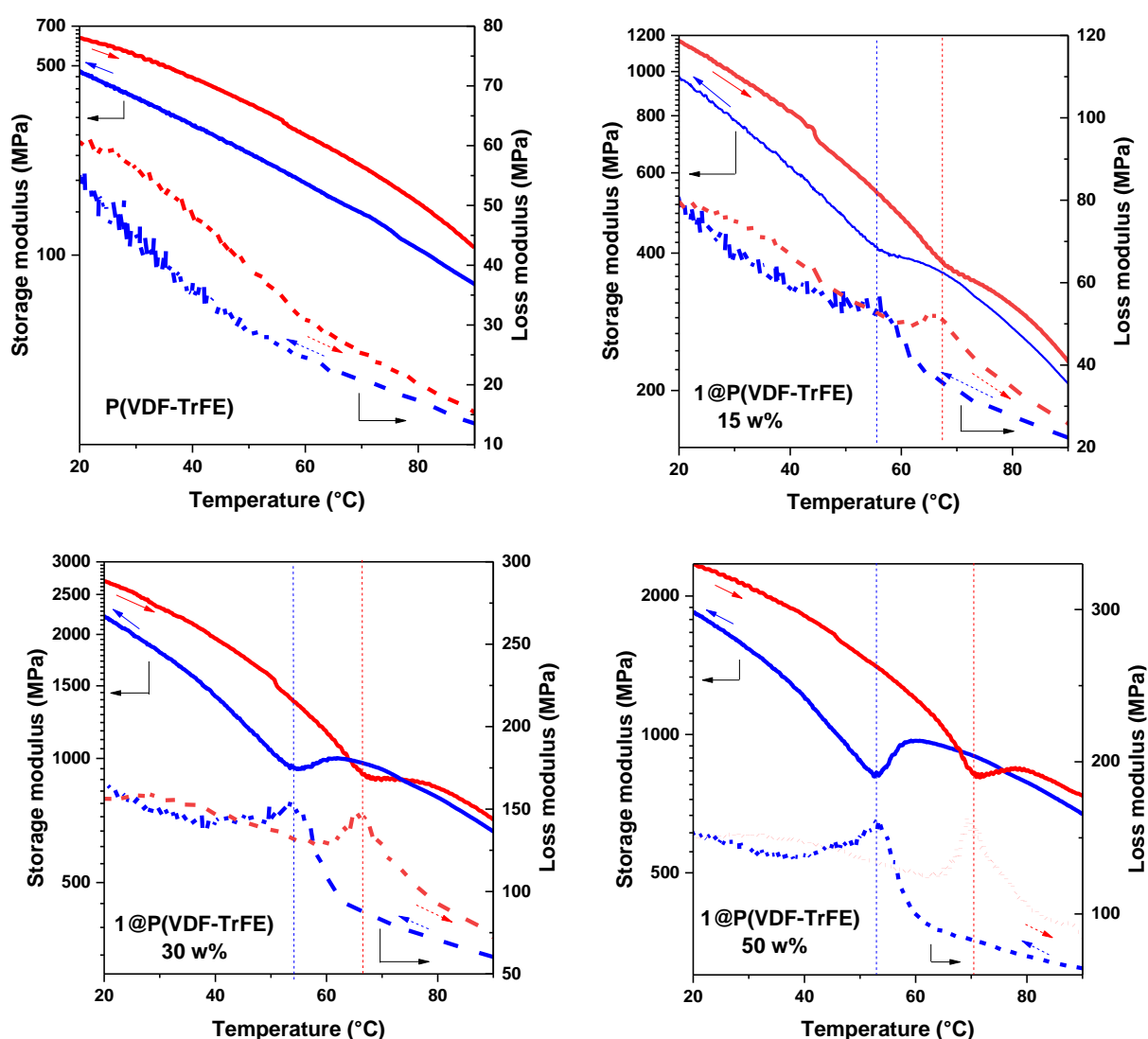


**Fig. 3.** Temperature dependence of the storage modulus (solid lines) and loss modulus (dashed lines) of the **1**@PVDF-TrFE// composites for particle concentrations of 0, 15, 30 and 50 wt. %. The SCO events are shown by vertical lines for heating (red) and cooling (blue).

One can also observe more pronounced storage modulus dips in the soft TPU composites, compared to the stiff P(VDF-TrFE) composites with the same particle concentration. For example, for the 50 wt. %, 1@TPU sample  $E'$  decreases abruptly from 530 MPa at 65 °C to 350 MPa at 55 °C, corresponding to 34 % drop, whereas in the 50 wt. % 1@P(VDF-TrFE) composite the change is only 20 %. On the other hand, the loss peaks do not show such marked differences between the two matrices. When comparing the different particle compositions, i.e., the 1@P(VDF-TrFE) and 2@P(VDF-TrFE) series (see Figs. 3 and S6), one can note similar elastic anomalies, although in the latter sample the peaks/dips are sharper. Interestingly, this feature allows to reveal the occurrence of two well-resolved loss peaks – on both sides of the storage modulus minimum (see Figs. S6 and S9), suggesting that more than one mechanisms may contribute to the elastic anomalies.

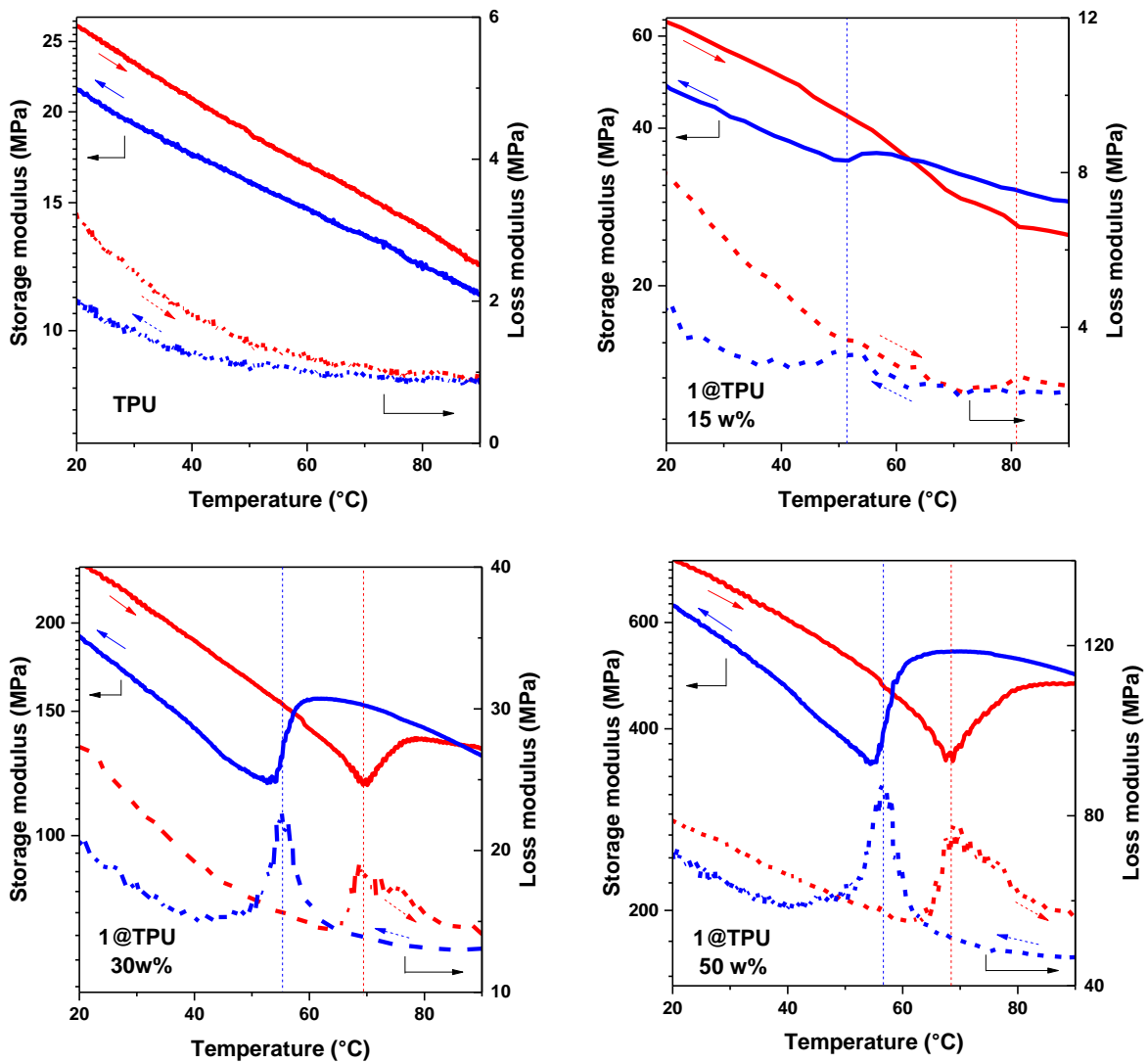


**Fig. 4.** Temperature dependence of the storage modulus (solid lines) and loss modulus (dashed lines) of the 1@TPU<sup>//</sup> composites for particle concentrations of 0, 15, 30 and 50 wt. %. The SCO events are shown by vertical lines for heating (red) and cooling (blue).

The elastic anomalies detected in our composite samples can be directly compared with those reported for the neat particle samples in ref. 52. Figure 5a shows variable frequency storage modulus and loss tangent data reported for the powder of **1**. Besides the obvious resemblance of the asymmetric shape of the storage modulus dip between the powder and composite samples, one can note also the negligible frequency dependence of the elastic softening effect in both samples (Figs. 5a-5b). This contrasts with the behavior of the loss peak, whose amplitude drastically decreases for increasing frequencies. Indeed, elastic anomalies accompanying phase transitions are known to display characteristic changes with the frequency of the applied mechanical stress ( $f$ ) and with the temperature scan rate of the experiment ( $dT/dt$ ).<sup>58</sup> To investigate the effect of the temperature scan rate, we compared DMA data obtained for a fixed temperature rate (3 K/min) with a thermogram constructed from a sequence of isothermal measurements (0 K/min) for the sample **1**@P(VDF-TrFE) (30 wt. %). The latter was achieved by keeping the sample at each temperature step for 3 min. As shown in Fig. 5c, the loss peak intensity is drastically reduced in isothermal conditions and the elastic softening becomes also less pronounced.

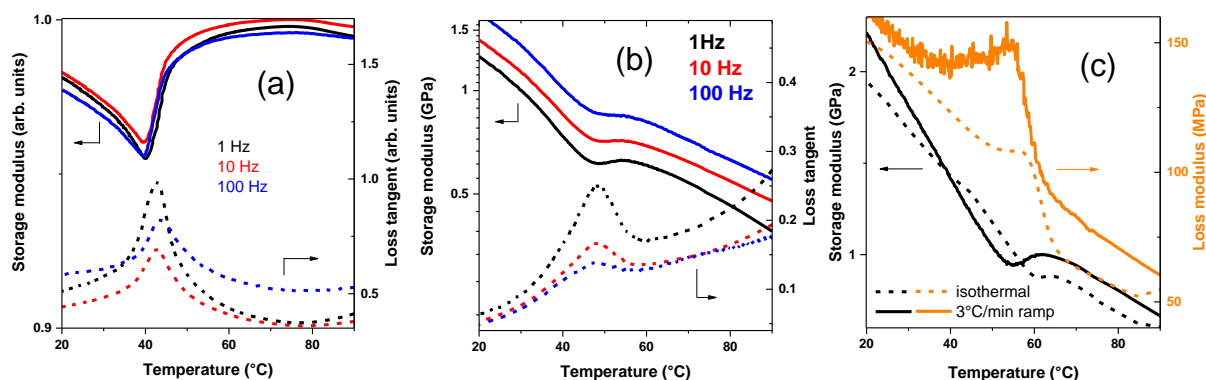


**Fig. 5.** Frequency dependence (1, 10 and 100 Hz) of the storage modulus (solid lines) and the loss tangent (dashed lines) for (a) the powder of **1** (data taken from ref. 52) and (b) the 30 wt. % **1**@P(VDF-TrFE) composite, acquired in the cooling mode. (c) Comparison of the temperature dependence of the storage and loss moduli of **1**@P(VDF-TrFE) (30 wt.%) obtained from a series of isothermal measurements and from a constant rate (3 K/min) thermal cycle.

**3.3. Transformation strain in the composites.** For mechanical applications, the main interest of our SCO@polymer composite samples is their ability to produce a spontaneous strain at the spin transition. The thermal expansion in the **1**@P(VDF-TrFE)<sup>//</sup> and **1**@TPU<sup>//</sup> composite films is displayed in Fig. 6 for different particle concentrations. (Data for the composites of compound **2**, as well as the ‘perpendicular cut’ samples, are shown in Figs. S10-S13.) Far from

the spin transition, the thermograms show ordinary linear thermal expansion, whereas the SCO phenomenon is characterized by abrupt changes and a thermal hysteresis of the strain. Following the first heating, this hysteresis becomes well reproducible. The transformation strain associated with the SCO phenomenon ( $\varepsilon^T$ ) is tabulated in Table 2 for the different samples. First, we note a neat correlation between the particle concentration and the effective strain, but the changes are not linear. There is a strong orientational anisotropy for composites of **1**, which systematically exhibit higher SCO strains in the ‘parallel cut’ samples. On the other hand, samples of **2** appear basically isotropic in this respect.

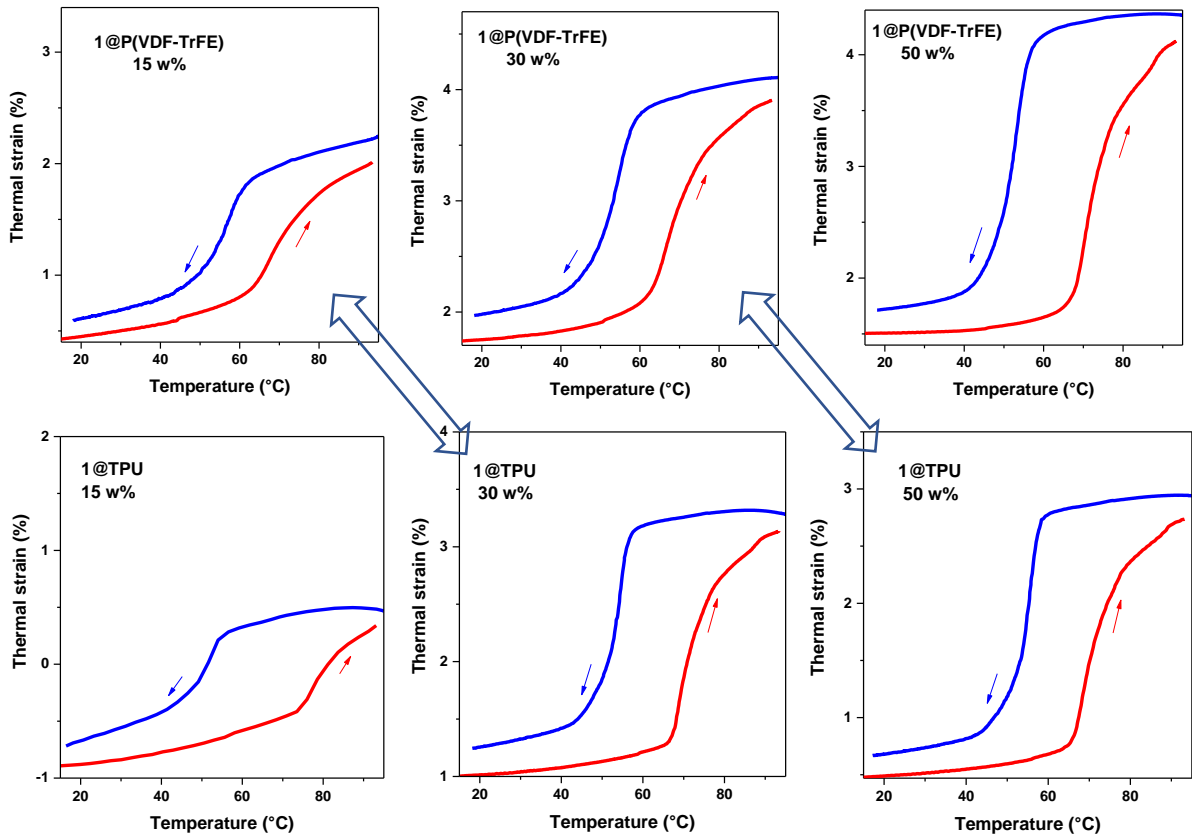


**Fig. 6.** Top panel: Thermal strain (2<sup>nd</sup> cycle) in the **1@P(VDF-TrFE)**// composites (15, 30 and 50 wt. %). Bottom panel: Thermal strain (2<sup>nd</sup> cycle) in the **1@TPU**// composites (15, 30 and 50 wt. %). Samples with similar particle volume fractions are connected by double-arrows.

From the data in Table 2, we can infer two key experimental findings. First, we observed systematically higher values of  $\varepsilon^T$  in the composites than what could be expected from the volume-weighted particle transformation strain. The transformation strain (ca. 5 %) in compound **1** occurs solely along the long axis of the particles.<sup>52</sup> If we take the example of the 16 vol. % **1@TPU** sample and we assume a perfect alignment of the particles (which is

obviously not the experimental case) one would expect maximum 0.8 % strain in the composite on a simple volumetric basis, which is only half of the measured value (1.7 %). The volumetric transformation strain in compound **2** is ca. 11 %.<sup>52</sup> Since the particles are randomly oriented in the composites, for a 28 vol. % **2**@P(VDF-TrFE) composite, the expectation on a volumetric basis would be  $\varepsilon^T = 1.0$  %, which is again inferior to the experimental value of 1.3 %. Besides, we have also observed a systematically higher transformation strain in the TPU matrix compared to P(VDF-TrFE), for similar particle volume fractions. As it will be discussed in section 4.2, these findings can be clearly rationalized by taking into account the particle – matrix elastic modulus contrasts in the different samples.

**Table 2.** Storage and loss moduli at 20 °C and the SCO-related transformation strain in the ‘parallel cut’ (//) and ‘perpendicular cut’ ( $\perp$ ) samples.

Sample	Particle vol. %	$E'_{20^\circ\text{C}}//$ (MPa)	$E''_{20^\circ\text{C}}//$ (MPa)	$\varepsilon^T//$ (%)	$E'_{20^\circ\text{C}}\perp$ (MPa)	$E''_{20^\circ\text{C}}\perp$ (MPa)	$\varepsilon^T\perp$ (%)
P(VDF-TrFE)	0	630	60	0	850	70	0
<b>1</b> @P(VDF-TrFE)	14	1200	80	0.9	1600	110	0.6
<b>1</b> @P(VDF-TrFE)	28	2700	160	1.6	2200	110	1.2
<b>1</b> @P(VDF-TrFE)	47	2300	150	2.4	2500	120	1.8
TPU	0	26	3	0	16	2	0
<b>1</b> @TPU	8	64	8	0.8	65	7	0.7
<b>1</b> @TPU	16	240	27	1.7	145	17	0.7
<b>1</b> @TPU	27	760	80	2.0	500	45	1.3
<b>2</b> @P(VDF-TrFE)	14	750	40	0.7	860	55	0.6
<b>2</b> @P(VDF-TrFE)	28	2000	95	1.3	1900	85	1.3
<b>2</b> @P(VDF-TrFE)	47	1600	110	1.8	1500	100	1.8

**3.4. Transformation stress in the composites.** Besides the stroke, another essential characteristic of an actuator is the stress it can generate. To investigate this property, thermal stress measurements were carried out, which consist in measuring the force generated when changing the temperature of the sample under an imposed constant tensile strain. Since the compressive thermal stress generated on heating tends to cancel the initial tensile stress, which maintains the sample stretched between the clamps, these measurements must be conducted using relatively large initial stresses. For this reason, one must use samples, which can resist to this stress and which produce relatively low thermal expansion. Taking into account these constraints, we could investigate only the **1**@P(VDF-TrFE)// composites with 15 and 30 wt. % particle concentrations (see Fig. 7 and Fig. S14). The transformation stress ( $\sigma^T$ ) associated with

the SCO phenomenon in these two samples is *ca.* 0.8 and 1.6 MPa, respectively. In agreement with our previous findings,<sup>51</sup> these values appear relatively small when considering the elastic modulus of these samples and the effective transformation strain (see Table 2). For example, in the sample **1**@P(VDF-TrFE) (30 wt. %), far from the spin transition, the ratio of thermal stress ( $\beta = 0.1 \text{ MPa}/^\circ\text{C}$ ) and thermal expansion ( $\alpha = 10^{-4} \text{ }^\circ\text{C}^{-1}$ ) coefficient is  $-\beta/\alpha = 1.0 \text{ GPa}$ , which can be interpreted as an effective modulus. On the other hand, the ratio of transformation stress and transformation strain at the SCO is only  $-\sigma^T/\varepsilon^T = 0.12 \text{ GPa}$ , denoting a significantly reduced effective modulus around the spin transition temperature. The correlation with the softening behavior of the storage modulus at the spin transition (Fig. 3) appears here very clearly.

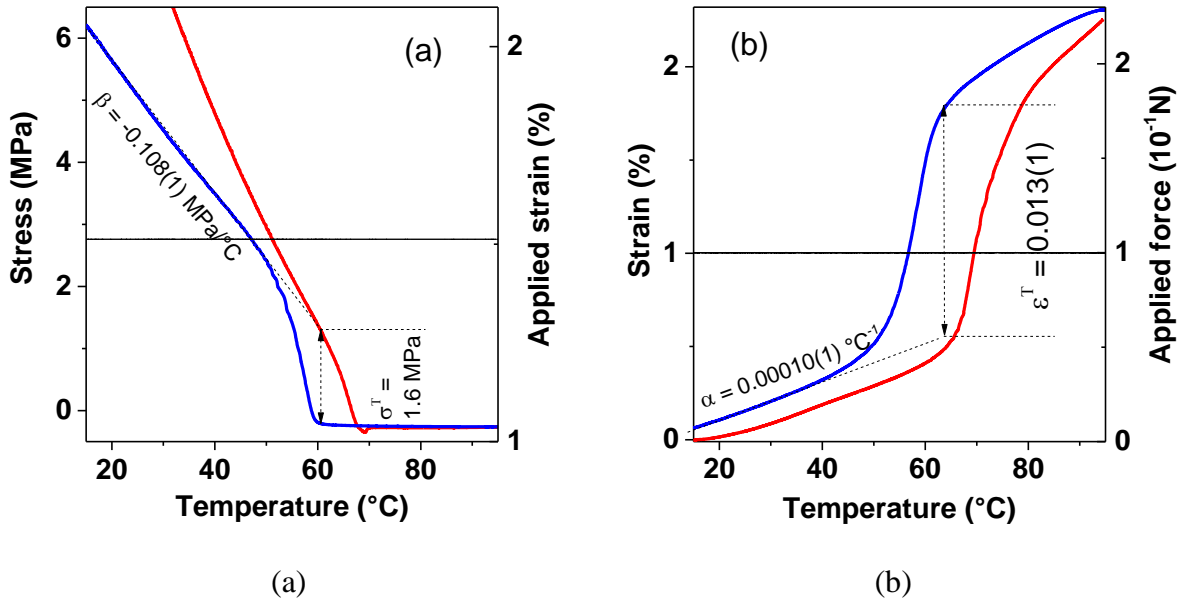


**Fig. 7.** (a) Stress under 1.5 % applied strain and (b) strain under 0.1 N applied force measured for a 30 wt. % **1**@P(VDF-TrFE)<sup>//</sup> composite over a complete thermal cycle (heating in red and cooling in blue). The applied stress and strain are shown in black. The ordinary thermal stress ( $\beta$ ) and thermal expansion ( $\alpha$ ) coefficients as well as the transformation stress ( $\sigma^T$ ) and strain ( $\varepsilon^T$ ) associated with the SCO phenomenon are also shown.

#### 4. Numerical modelling and discussion

In the following sections, we present numerical analysis and discussions of the two major experimental observations in our SCO@polymer composites, i.e. the elastic anomalies at the spin transition and the amplification (resp. reduction) of the transformation strain (resp. stress) in the soft matrices.

**4.1. Elastic softening and internal frictions at the spin transition.** Elastic anomalies accompanying phase transitions in different materials are ubiquitous and often spectacular due

to the drastic change of the structure and physical properties of matter in the vicinity of the transition temperature.<sup>58-60</sup> Such anelastic effects have been already reported for spin-state transitions in iron-bearing minerals and for a few molecular spin crossover complexes as well.<sup>52,61-65</sup> Since the volume of SCO materials differs in the two spin states, the proportion of HS and LS species will be modified to some extent by any externally applied stress. The spin-state of the material provides therefore an indirect link between stress and strain, in addition to the ordinary elastic response. Because the relaxation of the spin state of the system facilitates the deformation, the material appears softer near the spin transition temperature. In addition, since the relaxation process is irreversible, energy is dissipated giving rise to mechanical damping.

Carpenter and Salje discussed the elastic softening phenomena at structural phase transitions using the Landau formalism,<sup>59</sup> which was then adapted to analyze isostructural spin transitions as well.<sup>52,63</sup> Here we used a different approach, described by Wu et al.<sup>61</sup>, based on the thermodynamics of regular solid solutions to estimate the magnitude of elastic softening in compounds **1** and **2**. This phenomenological model is better suited for quantitative modeling of thermodynamical properties, even if the description of the SCO phenomenon remains rather simplified. We start our analysis from the well-known Gibbs free energy expression proposed by Slichter and Drickamer,<sup>66</sup> including a phenomenological nonlinear term  $\Gamma n(1 - n)$ , which describes deviations from the ideal solid solution (see Section S1 in the SI for more details):

$$G(n, P, T) = nG_{LS}(P, T) + (1 - n)G_{HS}(P, T) + \Gamma n(1 - n) - TS_{mix}(n) \quad (2)$$

where  $G, S_{mix}, \Gamma, n, P, T$  are the Gibbs free energy, mixing entropy, interaction parameter, LS fraction, pressure and temperature, respectively. The condition for equilibrium  $\left(\frac{\partial G}{\partial n}\right)_{P,T} = 0$  yields:

$$T = \frac{-\Delta H - P\Delta V + \Gamma(1 - 2n)}{N_A k_B \ln\left(\frac{1-n}{n}\right) - \Delta S} \quad (3)$$

where  $k_B, N_A, \Delta H, \Delta S, \Delta V$  are the Boltzmann constant, Avogadro number, enthalpy, entropy, and volume changes associated with the SCO, respectively. Since the SCO phenomenon in **1** and **2** does not involve shear strains, the bulk modulus is the elastic constant of primary interest. The total volume is given by:

$$V = \left(\frac{\partial G}{\partial P}\right)_T = \left(\frac{\partial G}{\partial P}\right)_{n,T} = nV_{LS} + (1 - n)V_{HS} \quad (4)$$

The isothermal bulk modulus  $K_T \equiv -V(\partial P/\partial V)_T$  can then be obtained by taking the derivative of Eq. 4 with respect to pressure:

$$\frac{V}{K_T} = -\left(\frac{\partial V}{\partial P}\right)_T = n \frac{V_{LS}}{K_T^{LS}} + (1-n) \frac{V_{HS}}{K_T^{HS}} + (V_{HS} - V_{LS}) \left(\frac{\partial n}{\partial P}\right)_T \quad (5)$$

In the case of compound **1**, the experimental SCO curve can be satisfactorily simulated using equation 3 with  $\Delta H = 19500 \text{ J mol}^{-1}$ ,  $\Delta S = 58.2 \text{ J mol}^{-1} \text{ K}^{-1}$  and  $\Gamma = 6800 \text{ J mol}^{-1}$ , leading to an equilibrium temperature of  $T_{eq} = 337 \text{ K}$ . These enthalpy and entropy changes are in reasonable agreement with the reported calorimetry data.<sup>52</sup> Figure 8a shows the computed variation of the LS fraction versus temperature for compound **1** (see Fig. S15 for compound **2**). For comparison, the SCO curve of an ideal HS/LS solution (i.e.,  $\Gamma = 0$ ) is also shown. For the latter, the SCO occurs in a gradual manner over a broad temperature range, whereas in compound **1**, the phase transition is abrupt with thermal hysteresis behavior.

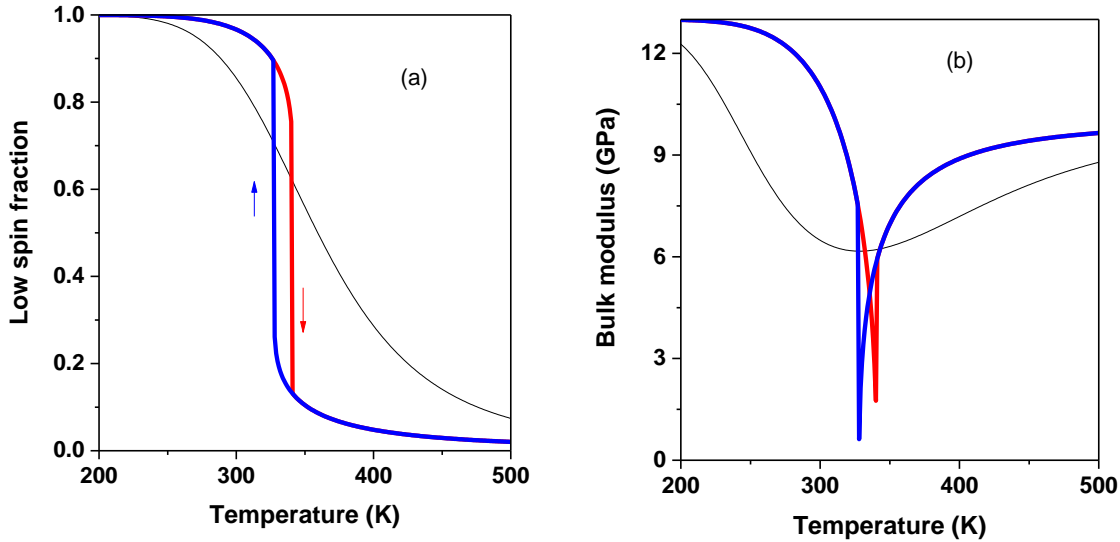


**Fig. 8.** (a) Simulation of the thermo-induced spin transition for compound **1** (heating in red, cooling in blue) and for an ideal solid solution (black). (b) Simulation of the concomitant changes of the bulk modulus.

Using equation 3, one can also compute the pressure dependence of the LS fraction and then assess the derivatives  $\left(\frac{\partial n}{\partial P}\right)_T$  for different temperatures. From previously published variable temperature and pressure crystallography data for **1**,<sup>52</sup> the volume in the LS state is  $V_{LS} = 3.9024e^{-4} \text{ m}^3 \text{ mol}^{-1}$ , the volume change at the SCO is  $\Delta V = 0.0462V_{LS}$  and the bulk modulus at 293 K is  $K = 13 \text{ GPa}$ . By injecting these data into equation 5, we computed the bulk modulus variation as a function of the temperature for **1**, as shown in Fig. 8b (see Fig. S15 for compound **2**). The bulk modulus exhibits considerable softening both for the gradual and abrupt SCO. For



the gradual conversion, the softening is less pronounced (ca. 50 %), but spans over a broad temperature range. For the abrupt spin transition, one can observe sharp dips of the bulk modulus at the transition temperatures, with values of  $K$  falling to  $\sim 1$  GPa. Compared to the bulk modulus at room temperature (13 GPa), this represents *ca.* one order of magnitude drop. Clearly, in the frame of our model, this softening arises because the depression of the bulk modulus is proportional to  $\left(\frac{\partial n}{\partial P}\right)_T$  (see Eq. 5). This calculation, based on the thermodynamics of solid solutions, remains of course just a crude, initial approach, neglecting notably the effects of phase separation. Nevertheless, it provides at least a gross estimate of the bulk modulus anomaly in the particles and confirms the importance of this phenomenon in modeling the thermomechanical properties of SCO@polymer composites.

From a mechanical perspective, anelastic behavior is a fully recoverable mechanism, but from a thermodynamic perspective it is irreversible. After an external perturbation, the associated approach to internal equilibrium is known as anelastic relaxation. The related energy absorption  $\Delta W$  during a cycle, divided by the maximum stored elastic energy  $W$  during that cycle, defines the inverse quality factor  $Q^{-1} = \Delta W/2\pi W$ , which is the most general measure of internal friction. An equivalent measure of the damping is the loss tangent, which is directly assessed from DMA measurements as the ratio of the loss and storage moduli:

$$Q^{-1} = \tan \varphi = \frac{E''}{E'} \quad (6)$$

The mechanical damping at the spin transition can be phenomenologically divided into three contributions:<sup>58</sup>

- 1) a transient component occurring under non-isothermal conditions and at sufficiently low frequencies. This component is related to the amount of transformed volume fraction per unit time  $\left(\frac{dn}{dt}\right)$  and appears dominant in our experimental conditions (see Fig. 5b and 5c).
- 2) a stationary component occurring under isothermal conditions. This part is also visible in Fig. 5c.
- 3) an intrinsic component, which is the algebraic average of the damping generated in the two coexisting phases. This contribution is expected to be minor in our case.

The interpretation of internal friction data is complicated by the fact that the mechanical damping may have various origins, such as intrinsic spin-state relaxation, interface motion, defects/dislocations-related relaxation phenomena, as well as static hysteresis.<sup>60</sup> For first-order transitions, most authors consider that the primary contribution to  $Q^{-1}$  at low frequencies

should arise from the motion of a phase interface across the sample.<sup>58</sup> Such mechanisms are indeed expected to occur in SCO single crystals wherein the coexistence of the HS and LS phases and the displacement of the interface(s) between them were repeatedly observed,<sup>67</sup> but the occurrence of a HS/LS interface in SCO nanoparticles remains an open question.<sup>68</sup> One additional source of internal friction may occur in SCO polymer composites, which arises from a change in the size and shape of the particles affecting particle-matrix interfacial properties. Further studies on bulk and composite samples displaying various types of SCO phenomena (gradual, abrupt) will be necessary to assess the importance of these different contributions.

**4.2. Effective transformation stress and strain at the spin transition.** Our goal is to provide general diagrams from which we can predict the overall mechanical behavior of the composite with varying SCO particle concentration, shape, orientation and contrast of mechanical properties between the matrix and the particles. The considered variations will cover a broad and relatively complete range of composites. For the calculations, our attention is restricted to the case of linear elastic problems in two-phase particulate composites, in which the spheroidal ( $a_1 = a_2 \neq a_3$ ) inhomogeneities could be distributed randomly or aligned (see Fig. 9), such that the overall behavior of the composite at the macroscale could vary from isotropic to transversely isotropic (see Section S2 for more details). Following the method discussed by Hashin<sup>55,69</sup> and McMeeking,<sup>56</sup> we have generalized their approach to compute the effective phase transformation stress,  $\boldsymbol{\sigma}^T$  and strain,  $\mathbf{e}^T$  in the two-phase composites with transversely isotropic base materials and spheroidal particles. To this end, first, we need to compute the effective bounds of mechanical properties, by choosing proper comparison media and calculating the Hill's tensor<sup>53</sup> (see Section S3 for more details). On the basis of the calculated Hashin-Shtrikman bounds<sup>70</sup> of effective mechanical properties (see Section S4 for more details), we can then compute the effective thermal expansion coefficients or effective transformation strains and stresses in the composite (see Section S5 for more details). The formal basis of the method is outlined in detail in the SI, here we restate only the equations used to calculate  $\boldsymbol{\sigma}^T$  and  $\mathbf{e}^T$ . The elasticity law for the non-transforming polymer matrix is:

$$\boldsymbol{\sigma}_m = \mathbf{C}_m \mathbf{e}_m \quad (7)$$

where  $\boldsymbol{\sigma}$ ,  $\mathbf{e}$ , and  $\mathbf{C}$  are stress, strain and the stiffness matrices, respectively. The elasticity law for the transforming SCO particles before and after transformation is:

$$\boldsymbol{\sigma}_p = \mathbf{C}_p \mathbf{e}_p \quad (8)$$

$$\boldsymbol{\sigma}_p = \mathbf{C}_p (\mathbf{e}_p - \mathbf{e}_p^T) \quad (9)$$

where  $\mathbf{e}_p^T$  is the homogeneous particle transformation strain. The subscripts  $m$  and  $p$  denote matrix and particles, respectively. The overall behavior of the particulate composite before and after transformation is determined by

$$\boldsymbol{\sigma} = \mathbf{C}\mathbf{e}^0 \quad (10)$$

$$\boldsymbol{\sigma} = (\mathbf{C}\mathbf{e}^0 - \mathbf{e}^T) \quad (11)$$

where  $\mathbf{e}^T$  is the effective transformation strain of the composite. Combining equations 7-11, an exact result for the overall phase transformation strain when the sample is free to expand can be obtained as:<sup>56</sup>

$$\mathbf{e}^T = \mathbf{C}^{-1}(\mathbf{C} - \mathbf{C}_m)(\mathbf{C}_p - \mathbf{C}_m)^{-1}\mathbf{C}_p\mathbf{e}_p^T \quad (12)$$

This equation refers to our thermal strain experiments shown in section 3.3. For the case that the material is completely fixed in all directions, the transformation stress is then computed as:

$$\boldsymbol{\sigma}^T = -\mathbf{C}\mathbf{e}^T = -(\mathbf{C} - \mathbf{C}_m)(\mathbf{C}_p - \mathbf{C}_m)^{-1}\mathbf{C}_p\mathbf{e}_p^T \quad (13)$$

In the case that the material is just fixed in the axial,  $x_3$  direction, as in our thermal stress experiments (see section 3.4), we have:

$$\boldsymbol{\sigma} = \begin{Bmatrix} 0 \\ 0 \\ \sigma_3 \\ 0 \\ 0 \\ 0 \end{Bmatrix}; \quad \mathbf{e} = \begin{Bmatrix} e_1 \\ e_2 \\ 0 \\ 0 \\ 0 \\ 0 \end{Bmatrix}; \quad \mathbf{e}^T = \begin{Bmatrix} e_1^T \\ e_2^T \\ e_3^T \\ 0 \\ 0 \\ 0 \end{Bmatrix} \quad (14)$$

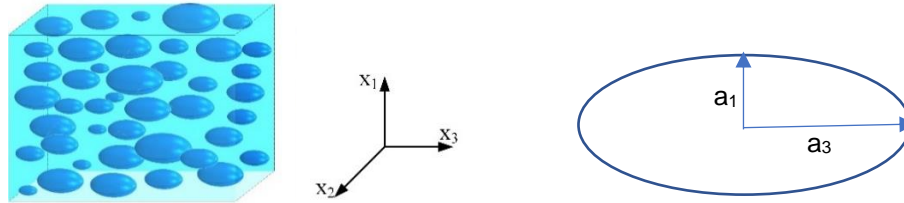


**Fig. 9.** Scheme of a composite with spheroids oriented in the  $x_3$  direction and definition of the particle aspect ratio using the minor and major semi-axes of the spheroid ( $a_1 = a_2$ )

As a starting point, we consider the  $\mathbf{1@P(VDF-TrFE)}$  composites, for which we possess the most complete data set, and we consider all particles aligned in the  $x_3$  direction as shown in Fig. 9. Despite considering the constituents isotropic, the overall behavior of the composite will be transversely isotropic due to the spheroidal shape of the particles, with the  $x_3$  axis as a normal axis to the plane of symmetry. The mechanical, thermal and phase transformation properties of this matrix and particles are given in Table 3. From TEM data (Fig. S4), the particle aspect ratio is estimated as  $\eta = \frac{a_3}{a_1} = 10$ . In the first calculations, the bulk modulus of the particles will be

assumed constant for simplicity, but in a second stage, the experimentally observed elastic softening will be also introduced. From a methodological point of view, we first compute the effective mechanical properties of the composites and then we use this information to calculate the effective phase transformation strains and stresses.

**Table 3.** Thermomechanical properties of  $[\text{Fe}(\text{NH}_2\text{trz})_3]\text{SO}_4$  and P(VDF-TrFE).  $K$ ,  $\nu$ ,  $\alpha$  and  $e_p^T$  stand for the bulk modulus, Poisson’s ratio, thermal expansion coefficient and particle transformation strain along the particle long axis.

Material	K (GPa)	K (GPa)	$\nu$	$\alpha \left( \frac{1}{^\circ\text{C}} \right)$	$e_p^T$
	T=20 °C	T=65 °C			
P(VDF-TrFE)	0.63	0.24	0.34	$7.45e^{-4}$	0
$[\text{Fe}(\text{NH}_2\text{trz})_3]\text{SO}_4$	13	13   1.0*	0.3	$5e^{-7}$	0.05

\* Considering elastic softening at the SCO (see Fig. 8b).

First, we analyze the effect of the contrast between the mechanical properties of the particles and the matrix. We define the dimensionless parameter  $K^* = \frac{K_p}{K_m}$ , which is the ratio of the bulk modulus of the particles to that of the matrix. In the case of an arbitrary isotropic mixture, there are no general results for the elastic moduli of a composite. Hence, bounds or estimates must be used. Figure 10a shows the variation of the elastic modulus  $k$  of the composite (see section S2 in the SI for the definition of  $k$ ) as a function of the particle volume fraction ( $\gamma_p$ ) calculated using the Hashin-Shtrikman bounds<sup>70</sup>. When the mechanical properties of two phases approach each other, i.e., when  $K^* \rightarrow 1$ , the bounds of mechanical properties become narrower until they coincide with each other. In this case, the effective behavior of the composite can be computed from a simple algebraic rule of mixtures. On the contrary, for  $K^* > 1$  and  $K^* < 1$  the uncertainty of the solution increases, i.e. the zone between the upper and lower bounds of the overall properties becomes wider. It is important to remark that the mechanical contrast,  $K^*$  governs not only the overall mechanical properties, but also the overall transformation stress and strain (see Eq. 12-13). This is seen both for the SCO-induced strain  $e_3^T$  when the sample is free to expand (Fig. 10b) and for the SCO-induced stress  $\sigma_3^T$  when the sample movement is constrained in the  $x_3$  direction (Fig. 10c). (See also Section S6 in the SI for more computational results.) As shown in Fig. 10b, when  $K^* > 1$ , the transformation strain  $e_3^T$  steadily increases for a given particle volume fraction. This finding explains obviously why we observe systematically higher transformation strain in the composites when compared to the volume-weighted particle

transformation strain as well as why the transformation strain is enhanced in the softer TPU matrix in comparison with the P(VDF-TrFE) (see Table 2). Remarkably, for  $K^* = 100$ , the value of  $e_3^T$  can potentially approach the maximum value of 0.05 for a particle volume fraction as small as 0.1.

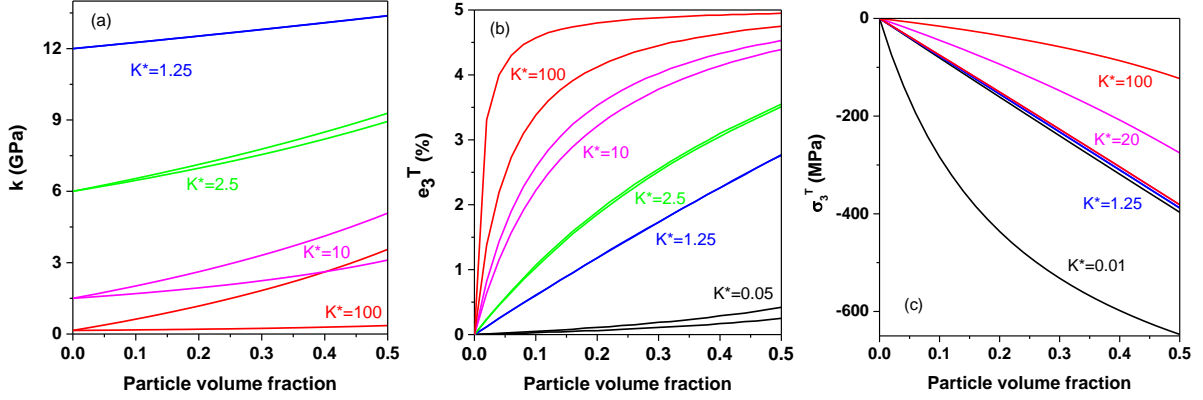


**Fig. 10.** Variation of the (a) effective elastic constant  $k$ , (b) transformation strain  $e_3^T$  and (c) transformation stress  $\sigma_3^T$  as a function of the particle volume fraction in composites of **1** for selected values of  $K^*$ . Particles are assumed to be aligned in the  $x_3$  direction. The matrix and particle properties are tabulated in Table 3.

Figure 10 also illustrates that as  $K^* \rightarrow 1$  (zero contrast between the mechanical properties) the effective transformation strain and stress in the composite will be simply the particle transformation strain multiplied by the particle volume fraction. On the other hand, when the matrix becomes much stiffer than the particles, i.e., when  $K^* \rightarrow 0$ , the transformation strain goes to zero. In summary, when the matrix becomes softer, the transformation strain induced by the particles can give rise to an enhanced deformation in the matrix and, as a result, in the composite. The price to pay, however, is a reduced transformation stress. In the opposite limit, a rigid matrix will resist against the deformation and most of the transformation strain converts to transformation stress. It may be worth noting here that  $\sigma_3^T$  in Fig. 10c was computed for a sample constrained only in the  $x_3$  direction. For a fully constrained sample, the resulting stress would be approximately doubled (see Fig. S24).

Figure 10 illustrates general tendencies, but the computed data does not match the measured values of  $e_3^T$  and  $\sigma_3^T$  for the experimental case of  $K^* = 17$  in **1**@P(VDF-TrFE). To reproduce the experimentally observed values, we need to consider two essential parameters, which are (i) the ‘true’ particle orientation within the composite and (ii) the softening of the elastic modulus of the particles (*vide supra*). Using the ImageJ software<sup>71</sup>, we have evaluated the average particle orientation in some of our samples using SEM images (see Fig. S5 for an

example). From the constant strain measurements shown in Fig. 7, we could also estimate the effective softening of the particles of **1** during the spin transition (see Table 3), whose validity was also supported by the simulations shown in Fig. 8. By introducing these two ingredients into our micromechanical model, we reevaluated the transformation stress and strain as a function of the particle volume fraction for our **1@P(VDF-TrFE)** composites, which are shown in Fig. 11. For completeness, this figure also displays the results obtained for fully aligned (in the  $x_3$  direction) and for randomly oriented particles. The computed data are now in reasonably good agreement with the experimental results, confirming notably the role of elastic softening in the effective mechanical behavior of SCO composite materials. These calculations can thus provide a valuable, quantitative tool to predict actuating properties of SCO@polymer composites. For example, for different applications, one may want to take advantage of either large values of produced strain or stress, which can be tuned by changing the  $K^*$  parameter. The effect of the particle aspect ratio and orientation on the overall properties of the composite are also crucial. The limiting case will be a composite filled with high aspect ratio ( $\eta \gg 1$ ) long fibers in the  $x_3$  direction. It is obvious that, in this case, the  $e_3^T$  can reach for low particle volume fractions the limiting value of 0.05, in particular for high values of  $K^*$  (see Fig. S24). Some further examples for the predicted thermomechanical behavior of SCO@polymer composites are given in Sections S6-S8 of SI.

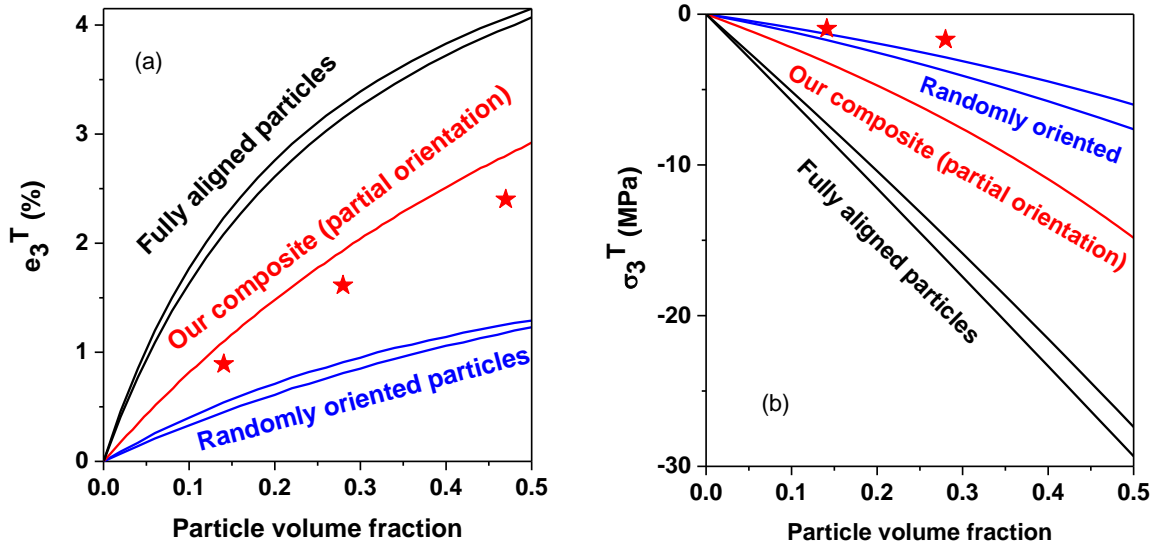


**Fig. 11.** Variation of the transformation strain  $e_3^T$  (a) and stress  $\sigma_3^T$  (b) as a function of the particle volume fraction in composites of **1@P(VDF-TrFE)** for different particle orientations (fully aligned, random and the experimental case) by considering the elastic softening of the particles. The matrix and particle properties are tabulated in Table 3. The experimental data are shown by red stars.

## 5. Conclusions

Using a combined experimental and theoretical approach, we have investigated the effective thermomechanical properties of spin-crossover@polymer composites made of different polymer matrices and SCO particles at various concentrations. The results allow us to reach two important conclusions. First, we confirmed our previous hypothesis<sup>21,51</sup> in that a soft (resp. stiff) matrix enhances the effective transformation strain (resp. stress), which is clearly demonstrated here by comparing soft TPU and stiff P(VDF-TrFE) matrices. We also show that these responses can be quantitatively predicted using appropriate micromechanics homogenization methods, which allow to assess also the impact of particle shape, orientation and concentration on the effective mechanical behavior of the composite upon the SCO phenomenon. Second, we uncovered significant anelastic phenomena in the composites, characterized by elastic softening and associated damping at the spin transition. We highlight that these effects are inherent properties of the SCO particles: they occur due to the sensitivity of the spin-state equilibrium to applied mechanical stress. We believe that the enhanced dissipation may be a useful asset in vibration damping applications.<sup>72</sup> On the other hand, the elastic softening phenomenon results in reduced actuating performance and should be therefore more quantitatively investigated on bulk SCO samples. Finally, this work also highlights that when SCO particles are embedded in an environment with a lower elastic modulus, the internal stresses generated at the spin transition remain too low to impact the SCO behavior sizeably. This might be different, however, if the particles are loaded into rigid environments, which should be investigated in further works.

## ASSOCIATED CONTENT

### Supporting Information

The Supporting Information is available free of charge online or from the author.

Schemes S1-S2: Compounds and samples. Table S1 and Figures S1-S14 additional DSC, thermorefectance, TEM, SEM and DMA data. Fig. S15 thermodynamical simulations for compound 2. Sections S1-S8 modelling methodology and additional computational results.

## AUTHOR INFORMATION

### Corresponding authors

Lionel Salmon - *LCC, CNRS & Université de Toulouse, 205 route de Narbonne 31077 Toulouse, France, [orcid.org/0000-0002-8064-8960](https://orcid.org/0000-0002-8064-8960); E-mail : [lionel.salmon@lcc-toulouse.fr](mailto:lionel.salmon@lcc-toulouse.fr)*

Gábor Molnár - *LCC, CNRS & Université de Toulouse, 205 route de Narbonne 31077 Toulouse, France, [orcid.org/0000-0001-6032-6393](https://orcid.org/0000-0001-6032-6393); E-mail : [gabor.molnar@lcc-toulouse.fr](mailto:gabor.molnar@lcc-toulouse.fr)*

Azzedine Bousseksou - *LCC, CNRS & Université de Toulouse, 205 route de Narbonne 31077 Toulouse, France, [orcid.org/0000-0002-1619-532X](https://orcid.org/0000-0002-1619-532X), E-mail : [azzedine.bousseksou@lcc-toulouse.fr](mailto:azzedine.bousseksou@lcc-toulouse.fr)*

### **Authors**

Seyed Ehsan Alavi - *LCC, CNRS & Université de Toulouse, 205 route de Narbonne 31077 Toulouse, France*

Baptiste Martin - *LCC, CNRS & Université de Toulouse, 205 route de Narbonne 31077 Toulouse, France*

Yue Zan - *LCC, CNRS & Université de Toulouse, 205 route de Narbonne 31077 Toulouse, France*

Xinyu Yang - *LCC, CNRS & Université de Toulouse, 205 route de Narbonne 31077 Toulouse, France*

Mario Piedrahita-Bello - *LCC, CNRS & Université de Toulouse, 205 route de Narbonne 31077 Toulouse, France*

William Nicolazzi - *LCC, CNRS & Université de Toulouse, 205 route de Narbonne 31077 Toulouse, France*

Jean-François Ganghoffer - *LEM3. Université de Lorraine, CNRS. 7, rue Félix Savart, 57070 Metz, France*

### **Author contributions**

SEA and BM contributed equally. Sample fabrication (YZ, MPB and LS), physical property measurements (BM, XY and GM), numerical simulations (SEA, JFG, WN and AB). All authors contributed to the data analysis and paper writing.

### **Conflicts of Interest**

The authors declare no conflicts of interest.

### **Data Availability Statement**



The data supporting this study's findings are available from the corresponding author upon reasonable request.

## ACKNOWLEDGMENTS

This project has received funding from the European Research Council (ERC) under the European Union's Horizon 2020 research and innovation program (grant agreement No. 101019522). YZ and XY thank the China Scholarship Council for their Ph.D. grants.

## REFERENCES

- (1) Gütllich, P.; Hauser, A.; Spiering, H. Thermal and optical switching of iron (II) complexes. *Angew. Chem. Int. Ed. Engl.* **1994**, *33*, 2024-2054.
- (2) Halcrow, M. A. (Ed.) Spin-crossover materials: properties and applications. John Wiley & Sons, Chichester, 2013.
- (3) Gütllich, P.; Goodwin, H. A. (Eds.) Topics in Current Chemistry: Spin Crossover in Transition Metal Compounds I-III, Springer, Heidelberg, 2004.
- (4) Bousseksou, A. (Ed.) Spin crossover phenomenon, In C. R. Chim., Publications de l'Académie des sciences, 2018.
- (5) Guionneau, P. Crystallography and spin-crossover. A view of breathing materials. *Dalton Trans.* **2014**, *43*, 382-393.
- (6) Grzywa, M.; Roß-Ohlenroth, R.; Muschielok, C.; Oberhofer, H.; Blachowski, A.; Zukrowski, J.; Vieweg, D.; Krug von Nidda, H.-A.; Volkmer, D. Cooperative large-hysteresis spin-crossover transition in the iron(II) triazolate [Fe(ta)<sub>2</sub>] metal-organic framework. *Inorg. Chem.* **2020**, *59*, 10501.
- (7) Collet, E.; Guionneau, P. Structural analysis of spin-crossover materials: From molecules to materials. *C. R. Chim.* **2018**, *21*, 1133-1151.
- (8) Pillet, S. Spin-crossover materials: Getting the most from x-ray crystallography. *J. Appl. Phys.* **2021**, *129*, 181101.
- (9) Manrique-Juarez, M. D.; Rat, S.; Salmon, L.; Molnar, G.; Quintero, C. M.; Nicu, L.; Shepherd, H. J.; Bousseksou, A. Switchable molecule-based materials for micro- and nanoscale actuating applications: Achievements and prospects. *Coord. Chem. Rev.* **2016**, *308*, 395-408.
- (10) Molnár, G.; Rat, S.; Salmon, L.; Nicolazzi, W.; Bousseksou, A. Spin crossover nanomaterials: from fundamental concepts to devices. *Adv. Mater.* **2018**, *30*, No. 1703862.

- (11) Salmon, L.; Catala, L. Spin-crossover nanoparticles and nanocomposite materials. *C. R. Chimie* **2018**, *21*, 1230–1269.
- (12) Mallah, T.; Cavallini, M. Surfaces, thin films and patterning of spin crossover compounds. *C. R. Chimie* **2018**, *21*, 1270-1286.
- (13) Enriquez-Cabrera, A.; Rapakousiou, A.; Piedrahita Bello, M.; Molnár, G.; Salmon, L.; Bousseksou, A. Spin crossover polymer composites, polymers and related soft materials. *Coord. Chem. Rev.* **2020**, *419*, No. 213396.
- (14) Shepherd, H. J.; Gural'skiy, I. Y. A.; Quintero, C. M.; Tricard, S.; Salmon, L.; Molnár, G.; Bousseksou, A. Molecular actuators driven by cooperative spin-state switching. *Nat. Commun.* **2013**, *4*, No. 2607.
- (15) Gural'skiy, I. A.; Quintero, C. M.; Costa, J. S.; Demont, P.; Molnar, G.; Salmon, L.; Shepherd H. J.; Bousseksou, A. Spin crossover composite materials for electrothermomechanical actuators. *J. Mater. Chem. C* **2014**, *2*, 2949–2955.
- (16) Piedrahita-Bello, M., Angulo-Cervera, J. E., Courson, R., Molnár, G., Malaquin, L., Thibault, C., Tondou, B., Salmon, L., Bousseksou, A. 4D printing with spin-crossover polymer composites. *J. Mater. Chem. C* **2020**, *8*, 6001-6005.
- (17) Manrique-Juarez, M. D.; Mathieu, F.; Laborde, A.; Rat, S.; Shalabaeva, V.; Demont, P.; Thomas, O.; Salmon, L.; Leichle, T.; Nicu, L.; Molnar, G.; Bousseksou, A. Micromachining-Compatible, Facile Fabrication of Polymer Nanocomposite Spin Crossover Actuators. *Adv. Funct. Mater.* **2018**, *28*, No. 1801970.
- (18) Angulo-Cervera, J. E.; Piedrahita-Bello, M.; Mathieu, F.; Leichle, T.; Nicu, L.; Salmon, L.; Molnar, G. ; Bousseksou, A. Investigation of the Effect of Spin Crossover on the Static and Dynamic Properties of MEMS Microcantilevers Coated with Nanocomposite Films of [Fe(Htrz)<sub>2</sub>(trz)](BF<sub>4</sub>)@P(VDF-TrFE). *Magnetochem.* **2021**, *7*, No. 114.
- (19) Piedrahita-Bello, M.; Angulo-Cervera, J. E.; Enriquez-Cabrera, A.; Molnar, G.; Tondou, B.; Salmon, L.; Bousseksou, A. Colossal expansion and fast motion in spin-crossover@ polymer actuators. *Mater. Horiz.* **2021**, *8*, 3055-3062.
- (20) Piedrahita-Bello, M.; Zan, Y.; Enriquez-Cabrera, A.; Molnar, G.; Tondou, B.; Salmon, L.; Bousseksou, A. Effect of the spin crossover filler concentration on the performance of composite bilayer actuators. *Chem. Phys. Lett.* **2022**, *793*, No. 139438.
- (21) Zan, Y.; Piedrahita-Bello, M.; Alavi, S. E.; Molnar, G.; Tondou, B.; Salmon, L.; Bousseksou, A. Soft Actuators Based on Spin-Crossover Particles Embedded in Thermoplastic Polyurethane. *Adv. Intell. Syst.* **2013**, in press, DOI: 10.1002/aisy.202200432.

- (22) Gros, C. R. ; Peprah, M. K. ; Felts, A. C. ; Brinzari, T. V. ; Risset, O. N. ; Cain, J. M. ; Ferreira, C. F. ; Meisel, M. W. ; Talham, D. R. Synergistic photomagnetic effects in coordination polymer heterostructure particles of Hofmann-like Fe(4-phenylpyridine)<sub>2</sub>[Ni(CN)<sub>4</sub>]·0.5H<sub>2</sub>O and K<sub>0.4</sub>Ni[Cr(CN)<sub>6</sub>]<sub>0.8</sub>·nH<sub>2</sub>O. *Dalton Trans.* **2016**, 45, 16624-16634.
- (23) Felts, A. C.; Andrus, M. J.; Knowles, E. S.; Quintero, P. A.; Ahir, A. R.; Risset, O. N.; LI, C. H.; Maurin, I.; Halder, G. J.; Abboud, K. A.; Meisel, M. W.; Talham, D. R. Evidence for Interface-Induced Strain and Its Influence on Photomagnetism in Prussian Blue Analogue Core–Shell Heterostructures Rb<sub>a</sub>Co<sub>b</sub>[Fe(CN)<sub>6</sub>]<sub>c</sub>·mH<sub>2</sub>O @K<sub>j</sub>Ni<sub>k</sub>[Cr(CN)<sub>6</sub>]<sub>l</sub>·nH<sub>2</sub>O. *J. Phys. Chem. C* **2016**, 120, 5420-5429.
- (24) Gros, C. R.; Peprah, M. K.; Hosterman, B. D.; Brinzari, T. V.; Quintero, P. A.; Sendova, M.; Meisel, M. W.; Talham, D. R. Light-induced magnetization changes in a coordination polymer heterostructure of a Prussian blue analogue and a Hofmann-like Fe (II) spin crossover compound. *J. Am. Chem. Soc.* **2014**, 136, 9846-9849.
- (25) Presle, M.; Maurin, I.; Maroun, F.; Cortès, R.; Lu, L.; Sayed Hassan, R.; Larquet, E.; Guiger, J.-M.; Rivière, E.; Wright, J. P.; Boilot, J.-P.; Gacoin, T. Photostrictive/Piezomagnetic Core–Shell Particles Based on Prussian Blue Analogues: Evidence for Confinement Effects? *J. Phys. Chem. C* **2014**, 118, 13186-13195.
- (26) Dia, N.; Lisnard, L.; Prado, Y.; Gloter, A.; Stéphan, O.; Brisset, F.; Hafez, H.; Saad, Z.; Mathonière, C.; Catala, L.; Mallah, T. Synergy in photomagnetic/ferromagnetic Sub-50 nm core-multishell nanoparticles. *Inorg. Chem.* **2013**, 52, 10264-10274.
- (27) Haraguchi, T.; Otsubo, K.; Sakata, O.; Fujiwara, A.; Kitagawa, H. Strain-Controlled Spin Transition in Heterostructured Metal–Organic Framework Thin Film. *J. Am. Chem. Soc.* **2021**, 143, 16128-16135.
- (28) Suleimanov, I.; Kraieva, O.; Costa, J. S.; Fritsky, I. O.; Molnár, G.; Salmon, L.; Bousseksou, A. Electronic communication between fluorescent pyrene excimers and spin crossover complexes in nanocomposite particles. *J. Mater. Chem. C* **2015**, 3, 5026-5032.
- (29) Boix-Constant, C.; García-López, V.; Navarro-Moratalla, E.; Clemente-León, M.; Zafra, J. L.; Casado, J.; Guinea, F.; Manas-Valero, S.; Coronado, E. Strain Switching in van der Waals Heterostructures Triggered by a Spin-Crossover Metal–Organic Framework. *Adv. Mater.* **2022**, 34, No. 2110027.
- (30) Koo, Y. S.; Galán-Mascarós, J. R. Spin crossover probes confer multistability to organic conducting polymers. *Adv. Mater.* **2014**, 26, 6785-6789.

- (31) Nieto-Castro, D.; Garces-Pineda, F. A.; Moneo-Corcuera, A.; Sanchez-Molina, I.; Galan-Mascaros, J. R. Mechanochemical processing of highly conducting organic/inorganic composites exhibiting spin crossover–induced memory effect in their transport properties. *Adv. Funct. Mater.* **2021**, *31*, No. 2102469.
- (32) Chen, C.; Meng, Y.; Ni, Z. P.; Tong, M. L. Synergistic electrical bistability in a conductive spin crossover heterostructure. *J. Mater. Chem. C* **2015**, *3*, 945–949.
- (33) Rat, S.; Piedrahita-Bello, M.; Salmon, L.; Molnár, G.; Demont, P.; Bousseksou, A. Coupling mechanical and electrical properties in spin crossover polymer composites. *Adv. Mater.* **2018**, *30*, No. 1705275.
- (34) Piedrahita-Bello, M.; Martin, B.; Salmon, L.; Molnar, G.; Demont, P.; Bousseksou, A. Mechano-electric coupling in P (VDF–TrFE)/spin crossover composites. *J. Mater. Chem. C* **2020**, *8*, 6042–6051.
- (35) Tondu, B.; Piedrahita-Bello, M.; Salmon, L.; Molnár, G.; Bousseksou, A. Robust linear control of a bending molecular artificial muscle based on spin crossover molecules. *Sens. Actuators A* **2022**, *335*, No. 113359.
- (36) Madden, J. D. W.; Vandesteeg, N. A.; Anquetil, P. A.; Madden, P. G. A.; Takshi, A.; Pytel, R. Z.; Lafontaine, S. R.; Wieringa, P. A.; Hunter, I. W. Artificial muscle technology: physical principles and naval prospects. *IEEE J. Oceanic Eng.* **2004**, *29*, 706–728.
- (37) Mirvakili, S. M.; Hunter, I. W. Artificial muscles: Mechanisms, applications, and challenges. *Adv. Mater.* **2018**, *30*, No. 1704407.
- (38) McCracken, J. M.; Donovan, B. R.; White, T. J. Materials as machines. *Adv. Mater.* **2020**, *32*, No. 1906564.
- (39) Ilami, M.; Bagheri, H.; Ahmed, R.; Skowronek, E. O.; Marvi, H. Materials, actuators, and sensors for soft bioinspired robots. *Adv. Mater.* **2021**, *33*, No. 2003139.
- (40) Yang, Y.; Wu, Y.; Li, C.; Yang, X.; Chen, W. Flexible actuators for soft robotics. *Adv. Intell. Syst.* **2020**, *2*, No. 1900077.
- (41) Asaka, K.; Okuzaki, H. (Eds.), *Soft Actuators*, Springer, Japan, 2014.
- (42) Li, M.; Pal, A.; Aghakhani, A.; Pena-Francesch, A.; Sitti, M. Soft actuators for real-world applications. *Nat. Rev. Mater.* **2022**, *7*, No. 235.
- (43) Majidi, C. Soft-matter engineering for soft robotics. *Adv. Mater. Technol.* **2019**, *4*, No. 1800477.
- (44) Apsite, I.; Salehi, S.; Ionov, L. Materials for smart soft actuator systems. *Chem. Rev.* **2021**, *122*, 1349–1415.

- (45) Zou, M.; Li, S.; Hu, X.; Leng, X.; Wang, R.; Zhou, X.; Liu, Z. Progresses in tensile, torsional, and multifunctional soft actuators. *Adv. Funct. Mater.* **2021**, *31*, No. 2007437.
- (46) Wang, J.; Gao, D.; Lee, P. S. Recent progress in artificial muscles for interactive soft robotics. *Adv. Mater.* **2021**, *33*, No. 2003088.
- (47) Higuera-Ruiz, D. R.; Nishikawa, K.; Feigenbaum, H.; Shafer, M. What is an artificial muscle? A comparison of soft actuators to biological muscles. *Bioinsp. Biomim.* **2021**, *17*, No. 011001.
- (48) Rat, S.; Nagy, V.; Suleimanov, I.; Molnar, G.; Salmon, L.; Demont, P.; Csoka, L.; Bousseksou, A. Elastic coupling between spin-crossover particles and cellulose fibers. *Chem. Commun.* **2016**, *52*, 11267-11269.
- (49) Tanasa, R.; Enachescu, C.; Laisney, J.; Morineau, D.; Stancu, A.; Boillot, M.-L. Unraveling the Environment Influence in Bistable Spin-Crossover Particles Using Magnetometric and Calorimetric First-Order Reverse Curves. *J. Phys. Chem. C* **2019**, *123*, 10120-10129.
- (50) Bibik, Y.; Angulo-Cervera, J. E.; Lampeka, R.; Gural'skiy, I. A. Tunable mechanical properties of [Fe(pyrazine){Au(CN)<sub>2</sub>]<sub>2</sub>–PVDF composite films with spin transitions. *Polymer* **2022**, *238*, No. 124410.
- (51) Angulo-Cervera, J. E.; Piedrahita-Bello, M.; Martin, B.; Alavi, S. E.; Nicolazzi, W.; Salmon, L.; Molnar, G.; Bousseksou, A. Thermal hysteresis of stress and strain in spin-crossover@ polymer composites: towards a rational design of actuator devices. *Mater. Adv.* **2022**, *3*, 5131-5137.
- (52) Paliwoda, D.; Vendier, L.; Getzner, L.; Alabarse, F.; Comboni, D.; Martin, B.; Alavi, S. E.; Piedrahita Bello, M.; Salmon, L.; Nicolazzi, W.; Molnár, G.; Bousseksou, A. Elastic properties of the iron(II)-triazole spin crossover complexes [Fe(Htrz)<sub>2</sub>trz]BF<sub>4</sub> and [Fe(NH<sub>2</sub>trz)<sub>3</sub>]SO<sub>4</sub>. *Cryst. Growth Des.* **2023**, *23*, 1903-1914.
- (53) Dvorak, G. J. Micromechanics of composite materials. Springer, Dordrecht, Heidelberg, New York, London, 2012.
- (54) Hill, R. A self-consistent mechanics of composite materials. *J. Mech. Phys. Solids* **1965**, *13*, 213-222.
- (55) Rosen, B. W.; Hashin, Z. Effective thermal expansion coefficients and specific heats of composite materials. *Int. J. Eng. Sci.* **1970**, *8*, 157-173.
- (56) McMeeking, R. M. Effective transformation strain in binary elastic composites, *J. Am. Ceram. Soc.* **1986**, *69*, C301–C302.

- (57) Piedrahita-Bello, M.; Ridier, K.; Mikolasek, M.; Molnár, G.; Nicolazzi, W.; Salmon, L.; Bousseksou, A. Drastic lattice softening in mixed triazole ligand iron (ii) spin crossover nanoparticles. *Chem. Commun.* **2019**, *55*, 4769-4772.
- (58) Pérez-Sáez, R. B.; Recarte, V.; Nó, M. L.; San Juan, J. Anelastic contributions and transformed volume fraction during thermoelastic martensitic transformations. *Phys. Rev. B* **1998**, *57*, No. 5684.
- (59) Carpenter, M. A.; Salje, E. K. Elastic anomalies in minerals due to structural phase transitions. *Eur. J. Mineral.* **1998**, *10*, 693-812.
- (60) Nowick, A. S.; Berry, B. S. Anelastic relaxation in crystalline solids, Academic Press, New York, London, 1972.
- (61) Wu, Z.; Justo, J. F.; Da Silva, C. R. S.; De Gironcoli, S.; Wentzcovitch, R. M. Anomalous thermodynamic properties in ferropericlase throughout its spin crossover. *Phys. Rev. B* **2009**, *80*, No. 014409.
- (62) Hsu, H.; Crisostomo, C. P.; Wang, W.; Wu, Z. Anomalous thermal properties and spin crossover of ferromagnesite (Mg,Fe)CO<sub>3</sub>. *Phys. Rev. B* **2021**, *103*, No. 054401.
- (63) Mason, H. E.; Li, W.; Carpenter, M. A.; Hamilton, M. L.; Howard, J. A.; Sparkes, H. A. Structural and spectroscopic characterisation of the spin crossover in [Fe(abpt)<sub>2</sub>(NCS)<sub>2</sub>] polymorph A. *New J. Chem.* **2016**, *40*, 2466-2478.
- (64) Jakobsen, V. B.; Trzop, E.; Dobbelaar, E.; Gavin, L. C.; Chikara, S.; Ding, X.; Lee, M.; Esien, K.; Müller-Bunz, H.; Felton, S.; Collet, E.; Carpenter, M. A.; Zapf, V. S.; Morgan, G. G. Domain Wall Dynamics in a Ferroelastic Spin Crossover Complex with Giant Magnetoelectric Coupling. *J. Am. Chem. Soc.* **2021**, *144*, 195-211.
- (65) Dobbelaar, E.; Jakobsen, V. B.; Trzop, E.; Lee, M.; Chikara, S.; Ding, X.; Müller-Bunz, H.; Esien, K.; Felton, S.; Carpenter, M. A.; Collet, E.; Morgan, G. G.; Zapf, V. S. Thermal and Magnetic Field Switching in a Two-Step Hysteretic MnIII Spin Crossover Compound Coupled to Symmetry Breakings. *Angew. Chem. Int. Ed.* **2022**, *61*, No. e202114021.
- (66) Slichter, C. P.; Drickamer, H. G. Pressure-induced electronic changes in compounds of iron. *J. Chem. Phys.* **1972**, *56*, 2142-2160.
- (67) Ridier, K.; Molnár, G.; Salmon, L.; Nicolazzi, W.; Bousseksou, A. Hysteresis, nucleation and growth phenomena in spin-crossover solids. *Solid State Sci.* **2017**, *74*, A1-A22.
- (68) Itoi, M.; Jike, T.; Nishio-Hamane, D.; Udagawa, S.; Tsuda, T.; Kuwabata, S.; Boukheddaden, K.; Andrus, M. J.; Talham, D. R. Direct observation of short-range structural coherence during a charge transfer induced spin transition in a CoFe Prussian

- blue analogue by transmission electron microscopy. *J. Am. Chem. Soc.* **2013**, *137*, 14686-14693.
- (69) Hashin, Z. Analysis of composite materials - a survey. *J. Appl. Mech.* **1983**, *50*, 481-505.
- (70) Hashin, Z.; Shtrikman, S. A variational approach to the theory of the elastic behaviour of multiphase materials. *J. Mech. Phys. Solids* **1963**, *11*, 127–140.
- (71) Schneider, C. A.; Rasband, W. S.; Eliceiri, K. W. NIH Image to ImageJ: 25 years of image analysis. *Nat. Methods* **2012**, *9*, 671–675.
- (72) Helbert, G.; Volkov, A.; Evard, M.; Dieng, L.; Chirani, S. A. On the understanding of damping capacity in SMA: From the material thermomechanical behaviour to the structure response. *J. Intell. Mater. Syst. Struct.* **2021**, *32*, 1167-1184.

## TOC Graphic

Dynamical Mechanical Analysis and Micromechanics Simulations of Spin-Crossover@Polymer Particulate Composites: Towards Soft Actuator Devices

Seyed Ehsan Alavi, Baptiste Martin, Yue Zan, Xinyu Yang, Mario Piedrahita-Bello, William Nicolazzi, Jean-François Ganghoffer, Lionel Salmon, Gábor Molnár, Azzedine Bousseksou

